Sensitivity, Accuracy and Limits of the Lightweight Three-Component SmartSolo Geophone Sensor (5 Hz) for Seismological Applications

Martin Zecka[1], Koen Van Noten[1], Thomas Lecocq[1]

[1]Royal Observatory of Belgium, Avenue Circulaire 3, 1180 Brussels, Belgium

Key Points:

- instrument tests
- nodal systems
- SmartSolo
- sensor performance

Corresponding author: M. Zeckra, `martin.zeckra@seismology.be`

Abstract

The use of Nodal systems based on autonomous geophone-based instruments entered the field of Seismology only recently. These lightweight solutions revolutionized seismological fieldwork through lightweight and wholistic instruments that are faster to deploy and easier to handle. The IGU-16HR series of SmartSolo® is one example, but yet lacking a thorough lab-based performance analysis. Here, we fill the knowledge gap, by performing a series of lab and field-based tests that focus on the sensors performance. The investigated parameters are the instruments transfer function, self-noise and overall performance to classical seismometer-based instruments. In the real-world application we show examples of H/V measurements of ambient vibrations in urban environments and the performance ranges with teleseismic waveform recordings. Under lab conditions, the nodal systems perform equally well as standard seismometers (e.g., Lennartz 3D/5s), even in the frequency range down to 0.2Hz, way below their natural frequency. The restitution can be carried out correctly with manufacturer given transfer function. At least for the vertical component, the instruments self-noise reaches the lower boundary of the global minimum noise level, confirming the ability to properly record teleseismic phases down to 0.1 Hz. In ambient noise studies the instrument limits are already reached at 0.8 Hz, but still resolve the fundamental frequencies within the methods uncertainty ranges, based on classical instrument data. These versatile and easy-to-use nodal systems are useful and reliable for a wide range of seismological applications. In addition, their installation is faster and reduced prices open the doors towards Large N installations and research studies for groups that face limited financial budgets.

Introduction

Recent developments in seismological research have seen tremendous increases in sheer size of data throughout the last decade (Quinteros et al., 2021; Arrowsmith et al., 2022). This evolution has been accompanied by increasing computational power enabling the processing of such large data-sets (Ahrens et al., 2011; Bozdag et al., 2014; MacCarthy et al., 2020) and the introduction of Machine Learning techniques for seismological data processing (Bergen et al., 2019; Kong et al., 2019; Arrowsmith et al., 2022). On the hardware side, the introduction of low-cost geophone sensors (e.g., Raspberry Shake) often in combination with wholistic software/hardware solutions enabled data recording in unprecedented quantity of stations and for non-scientific audiences, for which the term "citizen science" has been introduced (Chen et al., 2020; Subedi et al., 2020; De Plaen et al., 2021; Calais et al., 2022). While the use of such low-cost instrument is limited and cannot cover the full range of seismological methods (Anthony et al., 2019), integrated nodal systems bear the potential to present a cost-efficient compromise of the performance in between citizen instruments and classical seismological sensors.

Nodal systems are common practice in active seismic experiments for exploration of hydrocarbon and other resources (Dean et al., 2018), in which numerous geophones (mostly single component instruments) are regularly spaced over a site of interest recording subsurface reflections of actively induced signals (e.g., explosive or sweep). Besides extending to three-component instruments, latest developments in geophone sensors for nodal installations saw major efforts in enhancing the level of autarky. To overcome issues of power supply, communication and time accuracy in remote locations, integrated nodal systems eliminate cable-based solutions and incorporate digitizer, data storage, GPS and battery in a single acquisition unit (Dean & Sweeney, 2019). The first commercially available node that also enabled continuous data recording was the Fairfield ZLand node (A. T. Ringler et al., 2018). This instrument is also eligible to be used for seismological research questions. With a fraction of the purchasing costs compared to standard seismological acquisition systems, the installation of so-called Large N arrays with 100s to 1000s of nodes became possible (Hand, 2014; Karplus & Schmandt, 2018; Roux et al., 2018; Brenguier et al., 2015). One of the first installations of such kind was realized in the Los Angeles basin with $\sim 13,000$ seismic stations covering an area of 16 x 16 km with three separated arrays and equidistant sensor spacing of 100m that enabled unprecedented spatial sampling of wavefield and site-characteristics (Castellanos & Clayton, 2021).

SmartSolo® recently released their IGU-16 series instruments. These geophone instruments with a 5 Hz natural frequency are available as single (IGU-16 1C) or three-component (IGU16-HR 3C) sensors and are equipped with 24 bits digitizers and GPS. Batteries are modular and available as High Capacity Battery or Standard Capacity Battery Packs which, together with the sensor, eventually provides a single, closed casing sensor. The total weight of the 3C (2.4 kg high capacity, 1.7 kg standard capacity battery) and size (10.3 x 9.5 x 18.7 cm) outperforms classical seismometer-digitizer set-ups. During the installation of larger surveys, the operator profits from the reduced man-power and time necessary. Due to the modular design of the nodes that allows the replacement of their spike base with a tripod battery base, these sensors' potential use becomes independent from the available surface structure in the survey area, i.e., urban environments with a high degree of sealing. In the last years, the SmartSolo node series have been increasingly used for Large N installations in the field of passive seismology (e.g. Obermann et al., 2022; Chmiel et al., 2019).

So far, a comprehensive study identifying the capabilities of geophone-based node sensors for seismological purposes has only been performed for the Fairfield ZLand sensors (A. T. Ringler et al., 2018), but is yet unavailable for the SmartSolo sensors. In this study we evaluate the SmartSolo instruments characteristics, performance and limits in order to justify their use in a variety of seismological applications. In a set of lab-based experiments we identify the sensors' transfer function, control the manufacturer's given poles and zeros, check the self-noise level, and compare the sensors with well-calibrated seismometers. After that, we show the performance of the sensors during field installations with two examples focusing on teleseismic waveforms and ambient seismic noise measurements.

Instrument tests

Instrument response derived from coherent waveforms

In the recording of ground shaking, a seismic sensor acts as a filter in the sense of a linear, time-invariant system (LTI) (Scherbaum, 2006) when translating it into electric voltages as an output signal. This alternation from input to output signal is represented through the system's frequency response function or the transfer function. The quantitative description of the LTI then allows us to restore the original input signal by applying signal restitution to the obtained waveforms without further knowledge of the physical processes going on inside the filter (Scherbaum, 2006). The transfer function is then characterized by the complex poles and zeros.

Havskov & Alguacil (2015) have shown that it is possible to estimate the transfer function of a seismometer by using the natural vibrations of the ground as a shaking table recorded with two closely installed sensors. For the SmartSolo sensors, the output signal is expected to be contaminated by instrument noise and thus, we applied the cross-spectrum method (Eq. 1). In this method, the output of seismometer 1 is the input of seismometer 2 as a linear system that presents a transfer function in the form of:

$$T_2(\omega) = T_1(\omega)\frac{P_{21}(\omega)}{P_{11}(\omega)} \tag{1}$$

with P_{21} as the cross-spectrum between the outputs of both sensors and P_{11} as the autopower spectrum of the output of sensor 1. Under the assumption the instrument response (as poles and zeros) given by the manufacturer is correct for sensor 1, we can estimate the unknown response of sensor 2. This is repeated for all instrument pairs.

The estimation of the instrument response parameters represented by its poles and zeros is a non-linear operation. Therefore, T_2 is identified through the optimization of the poles and zeros and fitting the theoretical response function to the observed transfer function presented in equation 1. The misfit function of the optimization is represented by the complex L2-norm.

In order to obtain highly correlated ground motions, 24 3C nodes have been closely co-located (in a so called 'huddle', Fig. 1c) in a regular grid of 1m x 1m overall extension close to the Uccle permanent station of the Belgian seismic network (international code BE.UCC, Royal Observatory of Belgium, 1985). The location within Brussels assured a high noise level. During the recording period a teleseismic earthquake could be recorded (M7.3, Japan, GEOFON Data Centre, 1993) that further guarantees strong correlation of the obtained wavefield.

The resulting poles for the instrument response estimation strongly converge towards the values given by the manufacturer ($-22.2111-22.2178i$, $-22.2111+22.2178i$), with half of the estimated transfer functions obtaining misfits below 5%. The weighted mean for poles below this misfit threshold differs by $-0.0559\mp0.0552i$ from the manufacturer given values. Considering only the results with misfits below 2%, the poles differ by $-0.0162\mp0.0158i$. Stronger misfit of the resulting transfer functions are foremost proportional to intersensor distances as the higher frequency sections of the recorded noise spectra de-correlate with increasing distance. This result could be reproduced for the horizontal components as well, with an overall greater spread of high misfit poles and zeros. This is likely due to the higher self-noise of the horizontal components (section 2.2) that leads to less coherent waveforms, as they show lower signal-to-noise ratio of the teleseismic phases and are more affected by tilt of the sensor that reduces the overall sensitivity. However, the limitation to results with misfits below 5% or 2% leads to the same range of differences between manufacturer and estimated poles and zeros as determined for the vertical component.

poles	$-22.2111 - 22.2178i$	$-22.2111 + 22.2178i$
zeros	$0i$	$0i$
sensitivity (@0 gain)		$76.7e3\frac{mV}{\frac{m}{s}}$
digitizer gain		3355.4428

Table 1. Instrument Response for a SmartSolo IGU-16HR-3C node represented by Poles and Zeros.

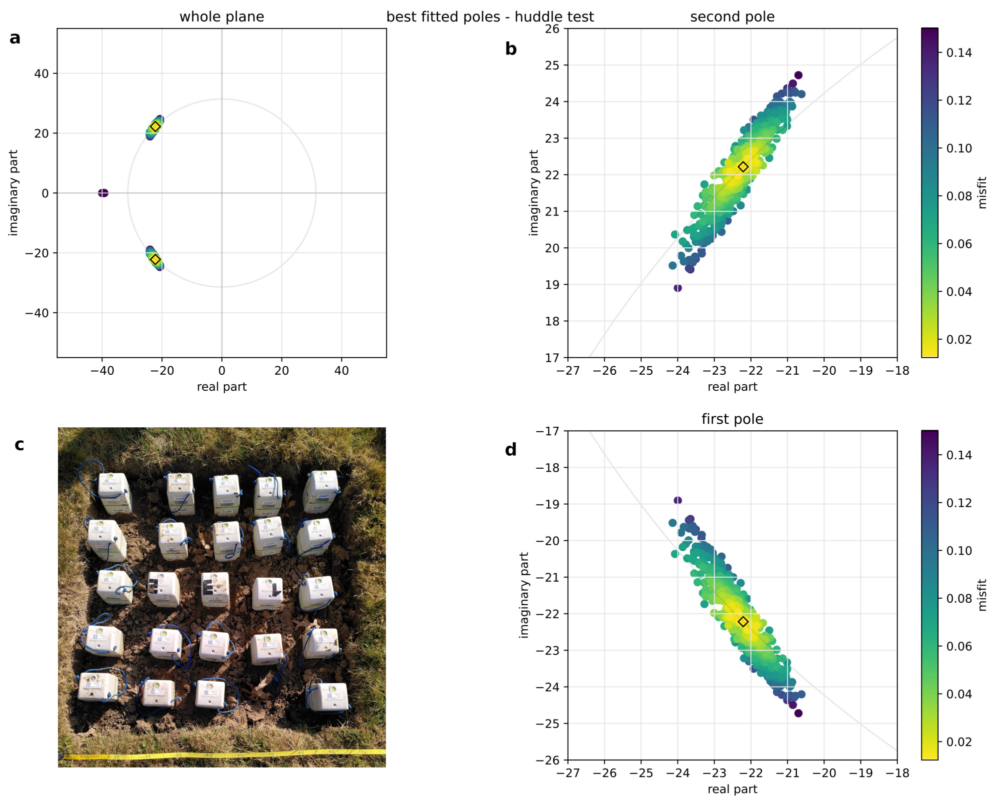

Figure 1. The resulting poles of the SmartSolo nodes huddle test, color-coded by misfit from the manufacturer's values, shown by the diamond marker. a) result shown over the whole complex plane that has been defined as the solution space in the inversion. b) and d) close-up view of the two poles. c) 24 nodes co-located during the huddle test. Note the slightly imperfect installation, contributing negatively to the misfit values.

Instrument self-noise and long-term noise stability

The experiment set-up presented in figure 1c of 24 co-located SmartSolo 3C instruments allowed us to apply the three instrument approach of Sleeman et al. (2006) to identify the instrument's self noise based on a common, coherent input data. Here, we rely on the analysis of actual ground motion recordings during the self-noise test. As the sensor and digitizer are located within the same casing, we cannot measure their self-noise independently and the full recording system combining both sensor and digitizer is analyzed. For the most part, the self noise of digitizers lies up to 20dB below the self noise of the sensors A. T. Ringler et al. (2014) and thus we assume that the obtained noise spectra will reflect only the sensor's self noise.

The comparison was performed for each instrument (i) using the two closest neighboring sensors of the grid (j, k). Similar to the huddle test, the use of the cross-spectrum (P_{ji}, P_{ik}, etc.) between the sensors eliminates the sensor's transfer functions and noise cross-spectra. The systems self-noise autospectrum (N_{ii}) then can be expressed solely through power- and cross-spectra of the obtained output of the three sensors (i, j, k) under the assumption of a common recording input as follows:

$$N_{ii} = P_{ii} - P_{ji} \cdot \frac{P_{ik}}{P_{jk}} \tag{2}$$

In order to retain comparability of the experiment outcome of A. T. Ringler et al. (2018)in which the authors performed a lab test for the Fairfield nodes on a shaking table and comparison with broadband sensors, we apply the same Fourier transformation parameters, prior downsampling (decimate from 250 to 50 Hz), and moving average to smooth the resulting spectra. The input data is a 1-hr period at a Thursday night (2022-03-17 01:30:00 UTC) in order to minimize the environmental noise close to the BE.UCCS station (lat 50.797, lon 4.36) in an open field as the spike at the bases could not be removed. In order to reduce errors propagating from transfer functions uncertainties, the input waveforms have been restituded (A. Ringler et al., 2011).

This following paragraph has been updated in version 3 and was faulty in the previous versions.

The resulting self-noise increases linearly between 0.7 to 15 Hz from around -140 dB to -130 dB (figure 2), which lies around the usual background noise of silent hard rock

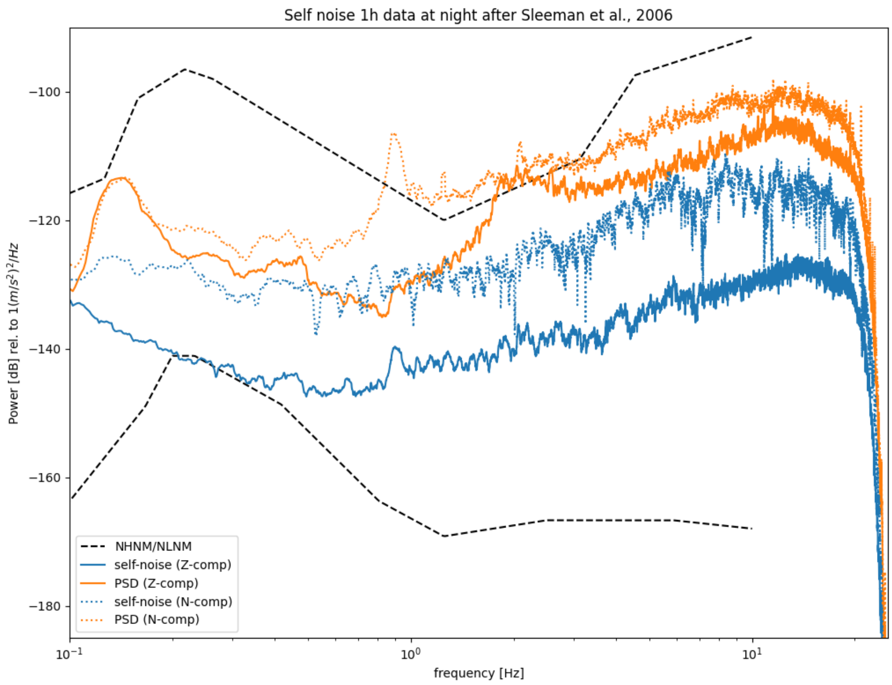

Figure 2. Outcome of the self-noise test following Sleeman et al. (2006). Blue curves is the estimated system self noise for a SmartSolo 3C sensor. Orange curves show the power spectrum of the recorded ground motion. The solid lines correspond to the vertical component and dashed colored lines show the equivalent for the North component. The black, dashed lines give the upper and lower global noise model bounds (Peterson, 1993).

stations in the Belgian network. For lower frequencies the self-noise is steadily increasing but remains around the NLNM until 0.2 Hz. For higher frequencies the self-noise is decreasing, due to the taper applied before the downsampling. The overall shape of the noise spectrum is comparable to the Fairfield nodes (A. T. Ringler et al., 2018), that was installed in the ASL underground vault and thus likely shows the true Fairfield self-noise. Above 1 Hz the SmartSolo node shows slightly higher noise-levels which corresponds to the nigher theoretical noise floor (3 - 16 dB). While for lower frequencies the SmartSolo node shows consistently lower self-noise that even reaches the NLNM levels (Peterson, 1993) and outperforms the Fairfield instrument. This observation underlines a decent sensitivity of the SmartSolo nodes for a seismological purpose as a passive sensor for temporal installations for recording ambient seismic noise, detecting local tectonic and/or induced earthquakes, investigating activity in geothermal fields, and they remain performant over a large frequency range from 5 s to their chosen Nyquist frequency (here 25 Hz). The increase in noise level towards the higher periods probably makes them less suitable to investigate teleseisms, microseism and storms.

The horizontal components show on average a 15 dB higher noise level that are more sensitive to signal distortion due to tilt. The cross- sensor comparison of all 24 installed instruments in the Huddle test experiment shows no major distortions or anomalies for individual instruments.Only a few nodes show some irregular higher variability of the elf-noise spectra. We suggest this might be related to the different level of coupling of each sensor that further introduces incoherencies in the recorded wavefields in the ambient noise frequency range. Such incoherence of the input of the three sensors is then further propagated into the noise spectrum analysis. In future analyses of the SmartSolo sensors this could be avoided by using a shaking table instead of relying on coherent waveform recordings. The three first generation instruments (indicated in figure 1c with the letters 1, 2, 3) installed alongside the newest generations show the same outcome.

Comparison with well-calibrated seismometers

	Güralp DM24 + 3ESP	CityShark II + Lennartz 3D	SmartSolo
natural/corner frequency	30 s	5s	5 Hz
sampling frequency	100 Hz	250 Hz	250 Hz
downsampled frequency	50 Hz	50 Hz	50 Hz

Table 2. Overview of seismometer and digitizer combinations with sampling specifications.

In a lab-based instrument test, the SmartSolo sensors were compared with well-calibrated, standard seismometers. The SmartSolo nodes were co-located with (i) the surface sensor of the Uccle station (network station code: BE.UCCS), that consists of a Güralp DM24/3ESP instrument, and (ii) with a Lennartz 3D sensor connected to a CityShark digitizer (Chatelain et al., 2000) for comparison to a standard instrument that is used for ambient seismic noise measurements (figure 3). During this experiment, we also investigated if the modular use of different base set-ups of the Smartsolo nodes al-

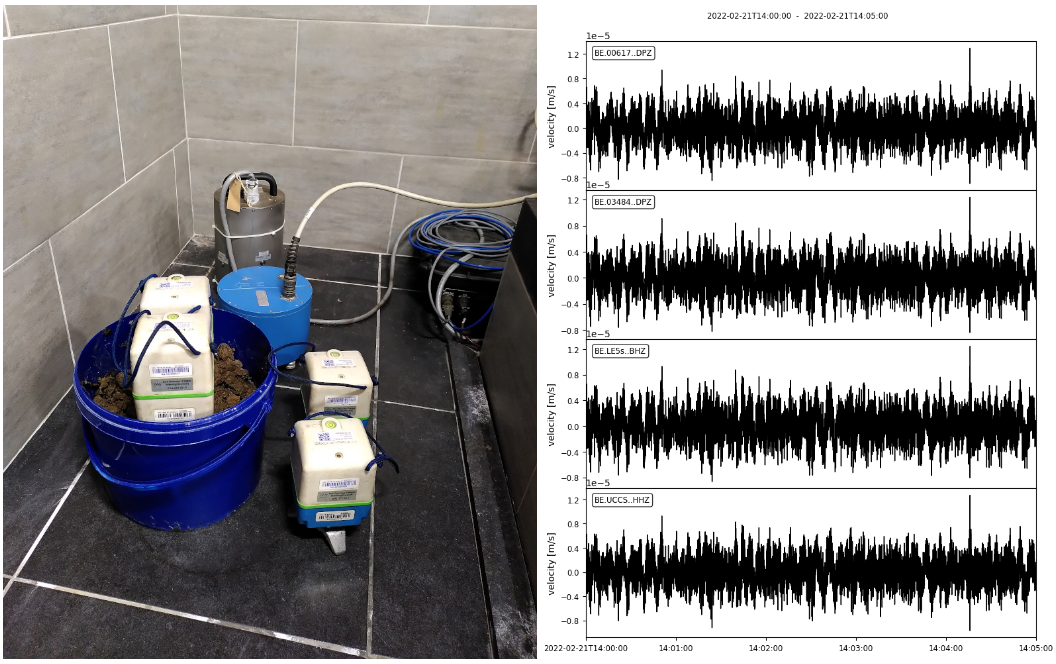

Figure 3. Co-location test of Smartsolo sensors with well-calibrated seismometers. Left: Two nodes each with different base set-ups either on a tripod or with a central spike in a sand-filled bucket, Lennartz LE3D/5s (blue instrument) connect to a Cityshark and Uccle surface station BE.UCCS (gray instrument in the back, Güralp CMG 3ESP). Right: restituted waveforms of all four kinds of sensors: From top to bottom: 1) node in bucket, 2) node on tripod, 3) LE3D/5s, 4) permanent sensor.

ters the recorded noise field. Two different set-ups were tested: (*i*) a 3C node connected to the High Capacity Battery Pack (gray) on a central spike installed in a sand-filled bucket and (*ii*) a 3C node connected to the Standard Battery Pack (blue) on a steel tripod base installed on the floor of the cave next to the listed seismometers above (figure 3).

To compare the obtained waveforms in the time and spectral domain, we first removed the instrument responses of all sensors (table 1). The restituted waveforms of all four sensor types are highly congruent in obtained ground velocity amplitudes and time accuracy. This congruence demonstrates the accuracy of the nodes' poles and zeros identified during the huddle test (see section above). In order to quantify the waveform similarity, we computed the coherence of all instrument combinations as the normalized cross-spectra (figure 4).

In comparison to the well-calibrated Güralp instrument, the node sensor installed on a tripod has the highest overall coherence with nearly perfect similarity from 20 Hz down to 10 s, way below its natural frequency (figure 4). A small deviation is present between 0.85 and 1.05 Hz that is more evident for the nodes with a central spike, but the waveform similarity always exceeds a 0.9 coherence. The decreasing coherence above 20 Hz for the SmartSolo sensors appears to be a filter artifact that propagates from the different decimation applied to the waveforms to result in a common sampling frequency (table 2). For the CityShark with Lennartz instrument the $\sim$ 1 Hz coherence drop is absent but above 4 Hz the waveform similarity to all other sensors in this test is steadily decreasing and falls below 0.9 at around 13 Hz. Due to the absence of a lowpass filter close to the Nyquist frequency of the raw data, we presume the existence of an analog filter in the CityShark digitizer with a cut-off that starts around 13 Hz and is not included in the instrument's transfer function.

The instrument comparison in the spectral domain is visualized in figure 4 and was obtained by dividing the power spectra of all instruments with all other instruments co-located during the experiment. Similar to the waveform similarity, we obtain flat spectral divisions at the ratio of 1 from ¿10 Hz down to less than 10s. Here, the similarity deviation around $\sim$ 1 Hz of the SmartSolo sensors becomes evident again and also is more pronounced for the sensors with a central spike installed in a sand-filled bucket. However, this effect can only be observed for the vertical components and is absent for the horizontal components. In the low frequency range below 0.2 Hz (remind that the node's natural frequency is 5 Hz) the horizontal spectra of the SmartSolo sensors deviate stronger from the spectrum obtained with the well-calibrated instrument as it can be observed for the vertical components. The deviation from the well-calibrated instrument is even larger for sensors that were installed with a spike in the sand-filled bucket and thus, results from the fact that the nodes were not fully buried and resulting in poorer leveling in comparison to the tripod based nodes.

Real-world observations (applications, sensitivity)

Teleseismic arrivals

In the previous chapter, it was shown that the waveforms obtained with the SmartSolo nodes bear the potential to recover ground motion far below their own natural fre-

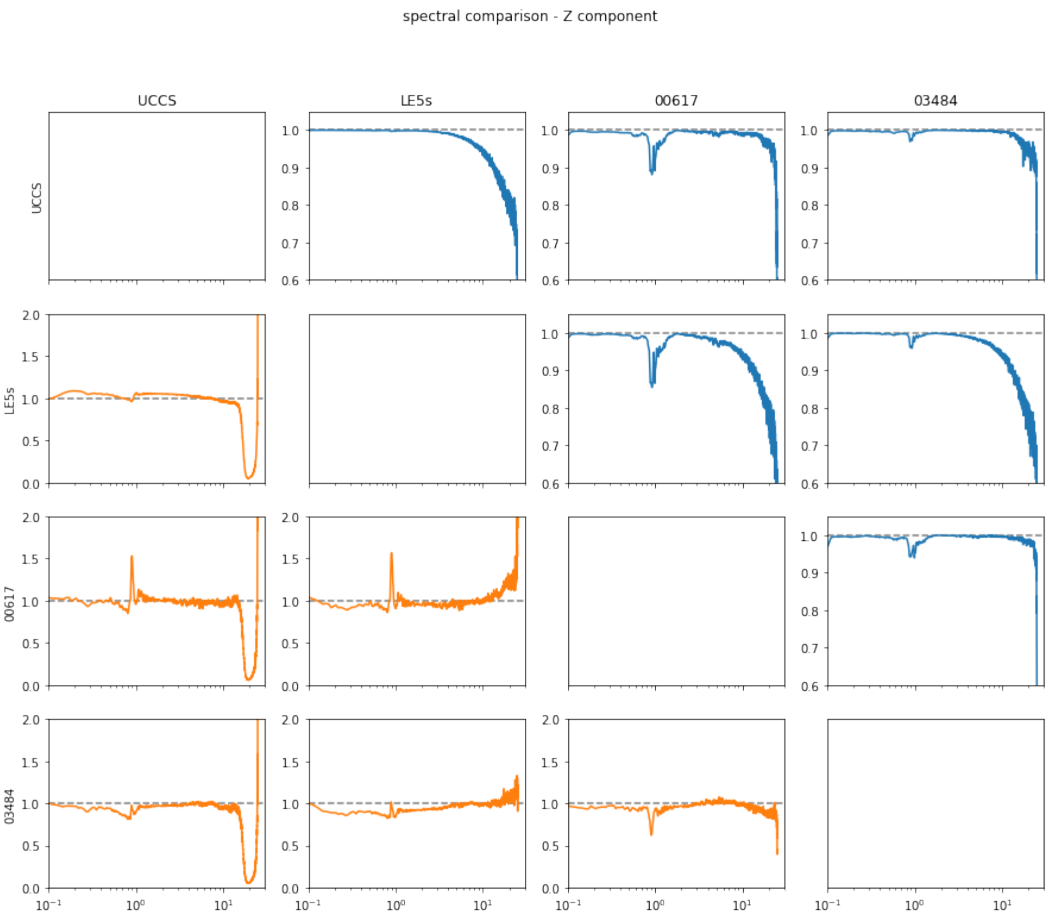

Figure 4. Waveform similarity between different types of sensors. Upper part (blue curves) shows the coherence amplitudes between the different sensors. Lower part (orange curves) gives the spectral divisions of all sensor combinations.

quency. During two longer term SmartSolo array installations in 2020 and 2022 around the BE.UCCS station, two teleseismic events in Kermadec (Mw 7.4, June 18, 2020) and Japan (Mw 7.3, March 16, 2022) respectively occurred during the surveys. To compare the node's performance with BE.UCCS, waveforms were first restituted to velocity and then bandpass filtered between 20 s and 3 s (figure 5).

The waveforms of the vertical component of a single Smartsolo sensor perfectly match the waveforms obtained with a Güralp instrument, with only slightly higher amplitudes for BE.UCCS. For both waveforms, the first arrivals of the body wave phases could be identified on a single vertical component for both events (PKIKP for Kermadec at 162° degree distance and PP for Japan at 84° distance). The surface waves of the 2022 Mw

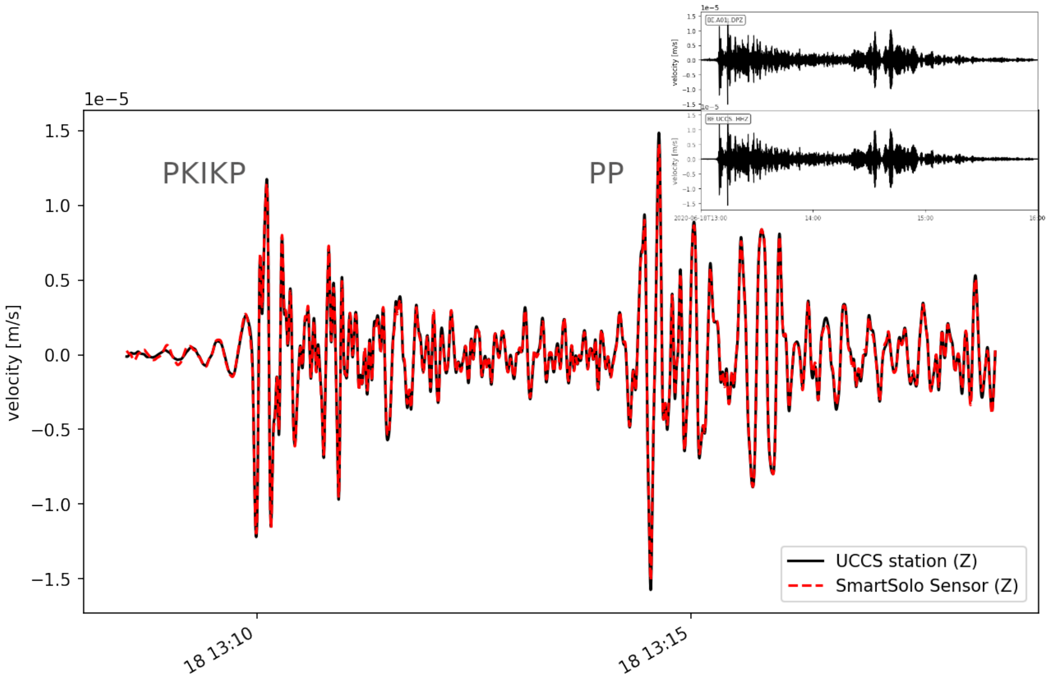

Figure 5. Teleseismic PKIKP and PP phases of the Mw 7.4 Kermadec earthquake (June 18, 2020) recorded with the vertical components at the BE.UCCS station (black) and with a single Smartsolo sensor (red). Both waveforms have been restituted to velocity and filtered between 20 s and 3 s. The inlet shows the full length (3 hours) of the teleseismic earthquake recorded with the SmartSolo Node (top trace) and the Güralp sensor (lower trace).

7.3 Japan earthquake could only be retrieved when lowering the bandpass filter down to 100 s, due to their lower dominant frequencies.

The horizontal components have a much reduced sensitivity in the very long period range. Thus for the Mw 7.4 Kermadec event, the earthquake can only be identified by stacking the waveforms of at least 20 nodes. It is important to mention that the station BE.UCCS around which the tests were performed is located in the city of Brussels and possesses one of the highest seismic noise levels in the whole BE network (Lecocq et al., 2020). In contrast, for the Mw 7.3 Japan earthquake, the first arrival S-phases and the surface waves can already be identified on a single horizontal sensor, but at the same cost as described before for the vertical component.

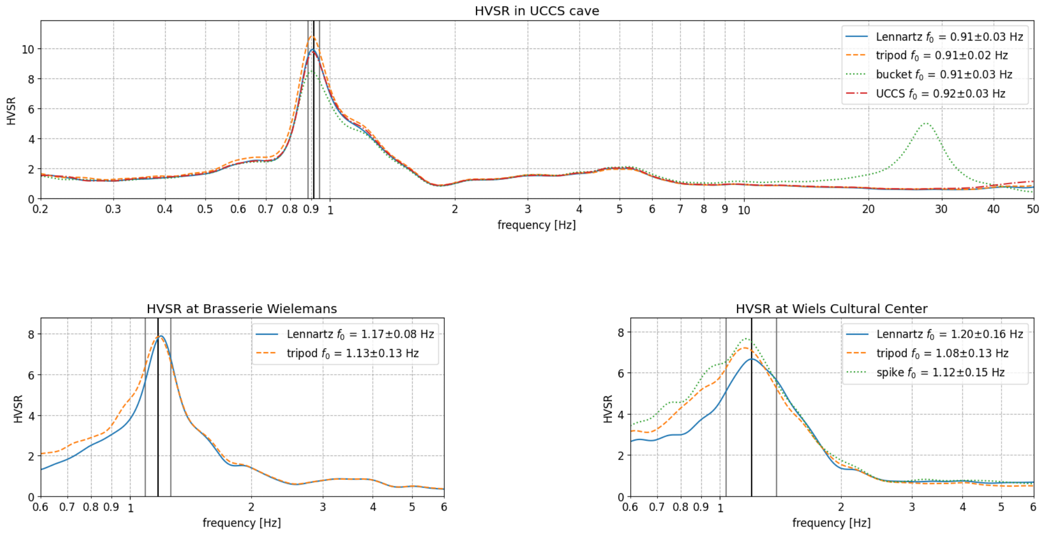

Figure 6. Instrument comparison through H/V analysis at three locations in Brussels. Waveforms have been restituted before the processing. HVSR graph from recordings a) at the location of UCC surface sensor (50.7973N, 4.3605E) from the sensor comparison lab test (fig. 3), with the blue solid line for LE3D-5s with Cityshark, orange dashed line for SmartSolo node on tripod base, green dotted line for node with spike in a sandfilled bucket and red dot-dashed line for Guralp permanent sensor. b) Location of the former Wielemans Brewery (50.8261N, 4.32646E) with LE3D-5s and Smartsolo sensors ∼10 cm apart. c) Location at the Wiels Cultural Center (50.82453N, 4.3259E) with LE3D-5s, node on tripod and node with spike digged into a grass field. Intersensor distance 5 - 10 m.

Ambient noise application

The preceding lab-based tests infer a suitable frequency range that justifies to use the SmartSolo sensors for passive measurements of ambient seismic noise in the frequency range of 0.2 to 25 Hz. As an example of an ambient noise application, we show three examples of Horizontal-to-Vertical Spectral Ratio (HVSR) (Nakamura, 1989; Molnar et al., 2022) surveys in Brussels, Belgium. In the framework of a shallow geothermal feasibility study, we prospected several sites in Brussels with non-invasive ambient noise observations prior to drilling. For the region of Brussels (Belgium), a conversion law exists to estimate the depth to bedrock from fundamental resonance frequency (f_0) values, derived from Horizontal-to-Vertical Spectral Ratio (HVSR) analysis of ambient noise measurements co-located with well logs (Van Noten et al., 2022). In the Brussels capital region, the main acoustic impedance contrast corresponds to a fundamental frequency range between 0.6 and 1.6 Hz (Van Noten et al., 2022).

At first, the data of the ideal case-study of the instrument comparison test (fig. 3) have been analyzed using Geopsy (Wathelet et al., 2020). The location of the permanent station (BE.UCCS) within the cave of the Royal Observatory of Belgium (ROB) reassures constant environmental conditions (e.g., stable temperature, no insulation). The circular street present around the ROB also provides sufficient distance and azimuthal coverage of anthropogenic noise sources. In this case study, the same time windows (120s long) have been used for all co-located instruments and the horizontal components have been averaged when computing the HVSR spectra. The HVSR spectra for all instruments (fig. 6a) are congruent for the most parts. The fundamental frequency f_0 can be reproduced by all sensors within 50% of the given uncertainty range (given as one standard deviation in Geopsy). For the HVSR amplitude at the f_0, the Lennartz seismometer (connected to the City-shark) is comparable to the UCCS, Güralp permanent sensor. The node on the tripod gives a 10% higher and the node in the bucket a 15% lower amplitude value. For frequencies above 13 Hz, the HVSR curve computed from the nodal instrument in the bucket deviates strongly and contains a second peak at 27.5 Hz. We presume this peak is related either to a bad coupling of the spike base in the sand-filled bucket, or to an impedance contrast between the bucket and the tiling floor with its concrete base. Considering the lower HVSR amplitude at f_0, the former is more likely as tilting shows stronger negative effects of the horizontal than the vertical components according to the manufacturer.

Under real-world conditions we present two examples from the southern part of Brussels. At the first location (fig. 6b), located next to the former *Brasserie Wielemans*, the Lennartz 5s with Cityshark and a SmartSolo node with a tripod base have been placed on a sidewalk, 10 cm apart. The street presents high traffic amounts, including public busses, streetcars and pedestrians passing next to the sensors. The second location, located 200m away from the first case (*Wiels Cultural Center*,fig. 6c) consists of a parking spot next to the same street and a community garden. That allowed us to install the Lennartz and tripod node next to a node with a spike for comparison. Distances between the sensors lie between 5 and 10 m. The f_0 values obtained at both locations are the same on average and given the uncertainties. This is expected as both locations show no elevation difference and have a samilar geologic subsurface structure located in the Sennevalley. Above 1.3 Hz the HVSR curves for each location are congruent. The shape of the HV peak for the *Brasserie Wielemans* is sharper and presents smaller uncertainties. The *Wiels* location demonstrates larger variations in f_0 as well as the corresponding amplitude.

The HVSR curves deviate strongly for frequencies below their f_0 peaks. The inspection of all analyzed time windows for the spectral analysis in Geopsy reveals much stronger fluctuation of the individual HVSR curves below 0.8 Hz. This leads to the wider average HVSR peak around f_0 in this frequency range. Below the S-wave resonance frequency the wavefield is dominated by body-waves and nearby sources (Lunedei & Malischewsky, 2015). In a densed urban area, as shown in the two examples, it might be impossible to decouple the instrument from the noise generating infrastructure (i.e., sidewalk of a heavily used street). In addition, noise-receiver distances are short and noise sources are non-stationary. Here, we recommend careful selection of investigation sites with longer recording periods and multiple locations. The impact of the noise instability below 0.8 Hz could be reduced through restitution of the raw waveform data. This step limits the amplitude differences of the mean HVSR curves as presented in figure 6.

The main distinction between the SmartSolo nodes and the classical seismometer-digitizer set-up became obvious in the handling of the hardware during the survey. The integrated node sensors outperform classical instruments in size, weight and usability. In the same time needed for one trained surveyor to install a seismometer-digitizer set-up, a single surveyor can transport and install up to 4 nodes. The use of multiple instruments might introduce some redundancy, but allows to capture potential lateral variations over short distances. Especially in urban contexts, additional sensors assure successful data recordings in cases of unwanted noise sources (e.g., traffic, pumps, etc.), unknown subsurface cavities (e.g., channels, sewers) or bad coupling (see above).

Conclusions

With three different “lab-based” tests using coherent ground motion recordings, we demonstrated the high performance of the 3C SmartSolo sensors (IGU-16HR-3C). The manufacturer given values for the transfer function could be reproduced in the so-called huddle-test and were used to accurately restitute the instrument responses. Their overall self-noise resides around the global minimum noise level (Peterson, 1993) over a wide frequency range, through which they become versatile and useful for a wide range of seismological applications, such as seismotectonics in local and regional distances, noise tomography, ambient noise studies and applied geophysics. In direct comparison to standard instruments in use for decades for seismological surveys, the nodes show at least the same performance levels, even beyond their natural frequency, while having the advantage of highly reduced purchasing costs, weight, and installation and dismantling time. This study endorses the use of SmartSolo nodes as low-budget alternatives, either for Large N installations or for research groups that have limited financial resources to perform seismotectonic or ambient noise studies using more expensive but higher-quality seismic sensors.

Data and Resources

All seismic waveforms processed for this study have been obtained at the Royal Observatory of Belgium and are available alongside with the publicly available python codes at `https://gitlab-as.oma.be/martinz/smartsolo-nodes-paper`.

Declaration of Competing Interests

The authors declare no competing interests.

Acknowledgments

The authors want to thank the staff of the Seismology-Gravimetry section at the Royal Observatory of Belgium for constructive discussions during various steps of the study. A special thanks goes to Giovanni Rapagnani for his help in data analysis and reviewing the manuscript. MZ has been funded by two projects of the Belgian Science Policy Office (BELSPO) including (1) the Belgian contribution to EPOS (FSIRI/33/EP1) and (2) the BRAIN-be 2.0 GeoCamb project (B2/191/P1/GEOCAMB).

References

Ahrens, J., Hendrickson, B., Long, G., Miller, S., Ross, R., & Williams, D. (2011). Data-intensive science in the us doe: case studies and future challenges. *Computing in Science & Engineering*, *13*(6), 14–24.

Anthony, R. E., Ringler, A. T., Wilson, D. C., & Wolin, E. (2019). Do low-cost seismographs perform well enough for your network? an overview of laboratory tests and field observations of the osop raspberry shake 4d. *Seismological Research Letters*, *90*(1), 219–228.

Arrowsmith, S., Trugman, D., MacCarthy, J., Bergen, K., Lumley, D., & Magnani, M. (2022). Big data seismology. *Reviews of Geophysics*, *60*(2), e2021RG000769.

Bergen, K. J., Chen, T., & Li, Z. (2019). Preface to the focus section on machine learning in seismology. *Seismological Research Letters*, *90*(2A), 477–480.

Bozdag, E., Lefebvre, M., Lei, W., Peter, D., Smith, J., Komatitsch, D., & Tromp, J. (2014). Big data and high-performance computing in global seismology. In *Egu general assembly conference abstracts* (p. 16606).

Brenguier, F., Kowalski, P., Ackerley, N., Nakata, N., Boué, P., Campillo, M., . . . Chaput, J. (2015, 11). Toward 4D Noise-Based Seismic Probing of Volcanoes: Perspectives from a Large-N Experiment on Piton de la Fournaise Volcano. *Seismological Research Letters*, *87*(1), 15-25. doi: 10.1785/0220150173

Calais, E., Symithe, S., Monfret, T., Delouis, B., Lomax, A., Courboulex, F., . . . others (2022). Citizen seismology helps decipher the 2021 haiti earthquake. *Science*, *376*(6590), 283–287.

Castellanos, J. C., & Clayton, R. W. (2021). The fine-scale structure of long beach, california, and its impact on ground motion acceleration. *Journal of Geophysical Research: Solid Earth*, *126*(12), e2021JB022462.

Chatelain, J.-L., Gueguen, P., Guillier, B., Frechet, J., Bondoux, F., Sarrault, J., . . . Neuville, J.-M. (2000). Cityshark: A user-friendly instrument dedicated to ambient noise (microtremor) recording for site and building response studies. *Seismological Research Letters*, *71*(6), 698–703.

Chen, K. H., Bossu, R., & Liang, W.-T. (2020). *The power of citizen seismology: Science and social impacts* (Vol. 8). Frontiers Media SA.

Chmiel, M., Mordret, A., Boué, P., Brenguier, F., Lecocq, T., Courbis, R., . . . Van der Veen, W. (2019, 05). Ambient noise multimode Rayleigh and Love wave tomography to determine the shear velocity structure above the Groningen gas field. *Geophysical Journal International*, *218*(3), 1781-1795. Retrieved from `https://doi.org/10.1093/gji/ggz237` doi: 10.1093/gji/ggz237

Dean, T., & Sweeney, D. (2019). Recent advances in nodal land seismic acquisition systems. *ASEG Extended Abstracts*, *2019*(1), 1–4.

Dean, T., Tulett, J., & Barnwell, R. (2018). Nodal land seismic acquisition: The next generation [Journal Article]. *First Break*, *36*(1), 47-52. doi: https://doi.org/10.3997/1365-2397.n0061

De Plaen, R. S., Márquez-Ramírez, V. H., Pérez-Campos, X., Zuñiga, F. R., Rodríguez-Pérez, Q., Gómez González, J. M., & Capra, L. (2021). Seismic signature of the covid-19 lockdown at the city scale: a case study with low-cost seismometers in the city of querétaro, mexico. *Solid Earth*, *12*(3), 713–724.

GEOFON Data Centre. (1993). *Geofon seismic network.* Deutsches GeoForschungsZentrum GFZ. Retrieved from `http://geofon.gfz-potsdam.de/doi/network/GE` doi: 10.14470/TR560404

Hand, E. (2014). *A boom in boomless seismology.* American Association for the Advancement of Science.

Havskov, J., & Alguacil, G. (2015). *Instrumentation in earthquake seismology.* Springer. (Publication Title: Instrumentation in Earthquake Seismology) doi: 10.1007/978-3-319-21314-9

Karplus, M., & Schmandt, B. (2018). Preface to the focus section on geophone array seismology. *Seismological Research Letters*, *89*(5), 1597–1600.

Kong, Q., Trugman, D. T., Ross, Z. E., Bianco, M. J., Meade, B. J., & Gerstoft, P. (2019). Machine learning in seismology: Turning data into insights. *Seismological Research Letters*, *90*(1), 3–14.

Lecocq, T., Hicks, S. P., Van Noten, K., Van Wijk, K., Koelemeijer, P., De Plaen, R. S., ... others (2020). Global quieting of high-frequency seismic noise due to covid-19 pandemic lockdown measures. *Science*, *369*(6509), 1338–1343.

Lunedei, E., & Malischewsky, P. (2015). A review and some new issues on the theory of the h/v technique for ambient vibrations. *Perspectives on European earthquake engineering and seismology*, 371–394.

MacCarthy, J., Marcillo, O., & Trabant, C. (2020). Seismology in the cloud: A new streaming workflow. *Seismological Research Letters*, *91*(3), 1804–1812.

Molnar, S., Sirohey, A., Assaf, J., Bard, P.-Y., Castellaro, S., Cornou, C., ... others (2022). A review of the microtremor horizontal-to-vertical spectral ratio (mhvsr) method. *Journal of Seismology*, 1–33.

Nakamura, Y. (1989). A method for dynamic characteristics estimation of subsurface using microtremor on the ground surface. *Railway Technical Research Insti-*

tute, Quarterly Reports, *30*(1).

Obermann, A., Sánchez-Pastor, P., Wu, S., Wollin, C., Baird, A. F., Isken, M. P., ... Wiemer, S. (2022, July). Combined Large-N Seismic Arrays and DAS Fiber Optic Cables across the Hengill Geothermal Field, Iceland. *Seismological Research Letters*. Retrieved 2022-08-17, from https://doi.org/10.1785/0220220073 doi: 10.1785/0220220073

Peterson, J. R. (1993). *Observations and modeling of seismic background noise* (Tech. Rep.). US Geological Survey. doi: 10.3133/ofr93322

Quinteros, J., Carter, J. A., Schaeffer, J., Trabant, C., & Pedersen, H. A. (2021). Exploring approaches for large data in seismology: User and data repository perspectives. *Seismological Research Letters*, *92*(3), 1531–1540.

Ringler, A., Hutt, C., Evans, J., & Sandoval, L. (2011). A comparison of seismic instrument noise coherence analysis techniques. *Bulletin of the Seismological society of America*, *101*(2), 558–567.

Ringler, A. T., Anthony, R. E., Karplus, M., Holland, A., & Wilson, D. C. (2018). Laboratory tests of three z-land fairfield nodal 5-hz, three-component sensors. *Seismological Research Letters*, *89*(5), 1601–1608.

Ringler, A. T., Sleeman, R., Hutt, C. R., & Gee, L. S. (2014). Seismometer self-noise and measuring methods. In *Encyclopedia of earthquake engineering* (pp. 1–13). Springer Berlin Heidelberg. doi: 10.1007/978-3-642-36197-5_175-1

Roux, P., Bindi, D., Boxberger, T., Colombi, A., Cotton, F., Douste-Bacque, I., ... Pondaven, I. (2018, 01). Toward Seismic Metamaterials: The METAFORET Project. *Seismological Research Letters*, *89*(2A), 582-593. doi: 10.1785/0220170196

Royal Observatory of Belgium. (1985). *Belgian seismic network.* International Federation of Digital Seismograph Networks. Retrieved from https://www.fdsn.org/networks/detail/BE/ doi: 10.7914/SN/BE

Scherbaum, F. (2006). *Of poles and zeros: Fundamentals of digital seismology* (Vol. 15). Springer Science & Business Media.

Sleeman, R., Van Wettum, A., & Trampert, J. (2006). Three-channel correlation analysis: A new technique to measure instrumental noise of digitizers and seismic sensors. *Bulletin of the Seismological Society of America*, *96*(1), 258–271.

Subedi, S., Hetényi, G., Denton, P., & Sauron, A. (2020). Seismology at school in nepal: a program for educational and citizen seismology through a low-cost seismic network. *Frontiers in Earth Science*, 73.

Van Noten, K., Lecocq, T., Goffin, C., Meyvis, B., Molron, J., Debacker, T. N., & Devleeschouwer, X. (2022). Brussels' bedrock paleorelief from borehole-controlled power laws linking polarised h/v resonance frequencies and sediment thickness. *Journal of Seismology*, *26*(1), 35–55.

Wathelet, M., Chatelain, J.-L., Cornou, C., Giulio, G. D., Guillier, B., Ohrnberger, M., & Savvaidis, A. (2020). Geopsy: A user-friendly open-source tool set for ambient vibration processing. *Seismological Research Letters*, *91*(3), 1878–1889.

Full mailing address for each author

Martin Zeckra - martin.zeckra@seismology.be

Koen Van Noten - koen.vannoten@seismology.be

Thomas Lecocq - thomas.lecocq@seismology.be